Aquarius RFI Detection and Mitigation Algorithm: Assessment and Examples

David M. Le Vine, *Life Fellow, IEEE*, Paolo de Matthaeis, *Member, IEEE*, Christopher S. Ruf, *Fellow, IEEE*, and David D. Chen

***Abstract*—Aquarius is an L-band radiometer system designed to map sea surface salinity from space. This is a sensitive measurement, and protection from radio frequency interference (RFI) is important for success. An initial look at the performance of the Aquarius RFI detection and mitigation algorithm is reported together with examples of the global distribution of RFI at the L-band. To protect against RFI, Aquarius employs rapid sampling (10 ms) and a "glitch" detection algorithm that looks for outliers among the samples. Samples identified as RFI are removed, and the remainder is averaged to produce an RFI-free signal for the salinity retrieval algorithm. The RFI detection algorithm appears to work well over the ocean with modest rates for false alarms (5%) and missed detection. The global distribution of RFI coincides well with population centers and is consistent with observations reported by the Soil Moisture and Ocean Salinity mission.**

***Index Terms*—Interference, microwave radiometry, remote sensing.**

I. Introduction

AQUARIUS is an L-band instrument designed to map the surface salinity field of the global oceans [1], [2]. It is the primary instrument on the Aquarius/SAC-D observatory, which is a partnership between the U.S. space agency National Aeronautics and Space Administration (NASA) and the Argentine space agency National Space Activities Commission (CONAE). The observatory was launched on June 10, 2011 from Vandenberg Air Force Base, Lompoc, CA, and Aquarius was turned on in late August [3]. It has been continuously operating since then. Among the special features of the radiometers are the provisions made for detecting and mitigating potential radio frequency interference (RFI). Although the radiometers are designed to operate in the spectral window at 1.413 GHz, which has been set aside for passive use only, the presence of RFI in this band has been well documented: RFI has been reported in airborne instruments operating in this band [4]–[6], and the recent observations of the radiometer aboard the Soil Moisture and Ocean Salinity mission (SMOS) [7], [8] confirmed that RFI in this band is a serious problem for remote sensing from space. The problem is particularly acute for remote sensing of salinity because of the relatively small dynamic range of the signal [9]. Over the open ocean, the change in salinity is relatively small (from about 32 to 37 on the practical salinity scale, i.e., 32–37 psu), which corresponds to a change in radiometric brightness temperature of a few Kelvin. Consequently, erroneous measurements due to undetected RFI can have a major impact on the accuracy of the retrieved salinity. A particular problem is interference from sources on land, which are strong enough to impact measurements while the sensor is over the ocean (see Section III).

In order to mitigate the effects of RFI, Aquarius employs rapid sampling and a "glitch detection" algorithm [10]. The algorithm has its heritage in a procedure designed to detect impulsive RFI such as due to radars, which are known to be a source of RFI in this band [11]. The goal was to sample much faster than the Nyquist rate for imaging (i.e., many samples in the time required for the antenna to move half the width of an image pixel) in the hope that samples corrupted with RFI could be identified and removed without having to discard data for the entire pixel. The glitch detector examines each short-time sample to detect outliers. The outliers are presumed to be associated with RFI and are removed from the data stream.

The objective of this paper is to describe the initial experience with the Aquarius RFI detection and mitigation algorithm and provide some examples of the global distribution of RFI at the L-band observed from space by Aquarius. Section II briefly describes Aquarius, and Section III presents examples of the global distribution of RFI observed by Aquarius. Then, Section IV presents an overview of the detection algorithm, and Section V discusses its performance including the false-alarm rate.

II. Aquarius

Aquarius is comprised of three L-band radiometers (1.41 GHz) and an L-band scatterometer (1.26 GHz) designed to work together to map the salinity field at the ocean surface from space [1]. The primary sensor for detecting changes in salinity is the radiometer. The scatterometer provides a correction for ocean surface roughness (waves), which is the primary source of error in the retrieval [12]. The radiometers operate in the spectral band at 1.41 GHz, which is relatively close to the peak in the sensitivity of thermal emission from the ocean surface to changes in salinity of the ocean water (which occurs near 600 MHz [9]). This frequency "window" is the largest piece of spectrum in this neighborhood protected from interference by man-made "noise" (i.e., RFI). Adequate spectrum, free of interference, is particularly necessary for remote sensing of salinity because of the extreme sensitivity

Manuscript received February 14, 2013; revised June 13, 2013; accepted July 4, 2013.

D. M. Le Vine and P. de Matthaeis are with the NASA Goddard Space Flight Center, Greenbelt, MD 20771 USA.

C. S. Ruf and D. D. Chen are with the University of Michigan, Ann Arbor, MI 48109 USA.

Color versions of one or more of the figures in this paper are available online at http://ieeexplore.ieee.org.

Digital Object Identifier 10.1109/TGRS.2013.2282595

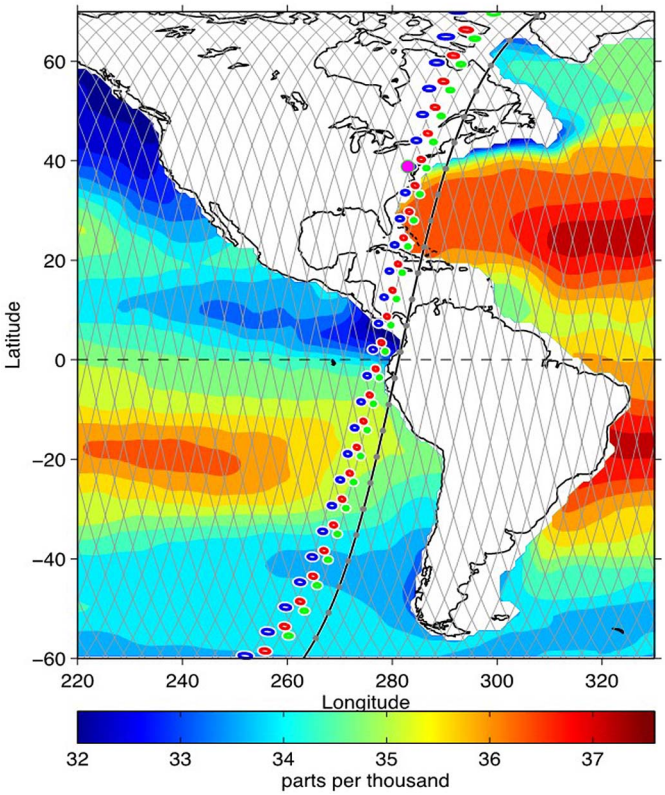

Fig. 1. Aquarius ground tracks showing the three radiometer footprints (colored dots) corresponding to the highlighted ground track of a descending orbit. The radiometers point westward roughly perpendicular to the ground track and pointing away from the Sun.

required for this measurement (about 0.1 K). For example, the science objective for Aquarius is to monitor the seasonal and interannual variation of the large-scale features of the surface salinity field in the open ocean by providing salinity maps on a monthly basis with a spatial resolution of 150 km and an accuracy of 0.2 psu [2]. Achieving an accuracy of 0.2 psu corresponds roughly to a radiometric accuracy of 0.1 K. This accuracy is achieved by a combination of internal calibration, careful thermal control, and averaging [1], [13].

The three Aquarius radiometer beams are arranged to image in a push-broom fashion with the boresight aligned roughly perpendicular to the spacecraft heading and pointing away from the sun. The three beams point at angles of 25.8°, 33.8°, and 40.3° with respect to the spacecraft nadir, which correspond to local incidence angles at the surface of 28.7°, 37.8°, and 45.6°, respectively. The radiometers measure vertical (V) and horizontal (H) polarizations, and the third Stokes parameter is obtained by detecting the sum and difference of the two polarizations (i.e., V $\pm$ H) and then taking the difference of the detected signals. Fig. 1 illustrates the imaging configuration of the radiometer showing the footprints on the surface (colored dots) relative to the satellite ground track (solid line). The spacecraft is in a sun-synchronous orbit with an equatorial crossing at 6 P.M. on the ascending side and an altitude of 657 km. At this altitude, the swath covered by the three radiometer beams is about 390 km, and the entire globe is mapped every seven days. The orbit is "frozen" such that the tracks repeat every seven days passing over the same location with an accuracy of about 10 km. Fig. 1 shows a descending pass with the Sun to the right and the imaged swath on the nighttime side of the ground track. This orientation was chosen to avoid radiation from the Sun as much a possible. (The Sun is a strong source of radiation at the L-band [14].)

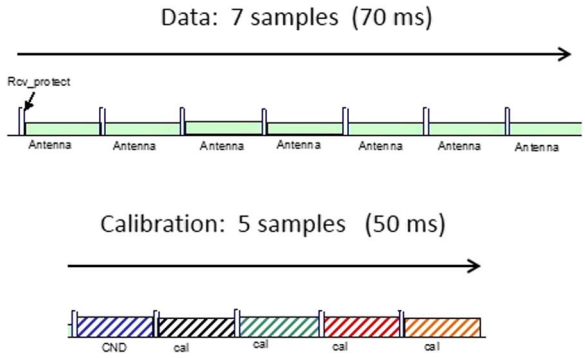

Fig. 2. Aquarius radiometer timing diagram. The radiometer is blanked during the first millisecond while the scatterometer transmits and collects data during the remaining 9 ms. This is repeated seven times (i.e., looking at the antenna for 70 ms) followed by five periods (50 ms) looking at one of several internal calibration references.

An important feature of the Aquarius approach to RFI detection and mitigation is rapid sampling. The goal is to obtain many samples in the time it takes for the radiometer to move one half the width of its along-track footprint (i.e., the Nyquist rate of the surface pixels). The fundamental Aquarius sample period is 10 ms, and the Nyquist rate is more than 5 s. The instrument timing diagram is shown in Fig. 2 (also see [1, Fig. 7]). The first 1 ms of the 10-ms period is reserved for the scatterometer transmit function. (The scatterometer and the radiometer share the same antenna feedhorns. During receive operations, a large filter is adequate to provide separation [1]; however, for the first millisecond, during the scatterometer transmit cycle, the radiometer is disconnected from the antenna for added protection.) Both the radiometer and the scatterometer receive during the remaining 9 ms. The complete cycle of radiometer data acquisition is a sequence of 12 such 10-ms intervals. The radiometer observes the scene for the first 7 of the 12 intervals. This is followed by five intervals of internal calibration (shown on the second line in the diagram) during which the radiometer is connected to one of several internal reference loads. Among the internal references is a "correlated noise diode" labeled CND in the diagram, which feeds both polarizations and is used for calibration of the third Stokes parameter. Because of limitations on data handling, only five of the seven antenna "data" samples are transmitted to the ground. The first two and the second two 10-ms data samples are averaged in hardware aboard the spacecraft before transmission to the ground. These five samples are called "short accumulations."

After transmission to the ground, the antenna data and calibration samples are separately processed. The data samples (short accumulations) go directly to the RFI algorithm, and the calibration samples go to a parallel algorithm where they are averaged and used to develop the counts-to-TA calibration and to determine the radiometer gain. The data arrive in groups (called subcycles) of 120 ms. After the RFI detection and

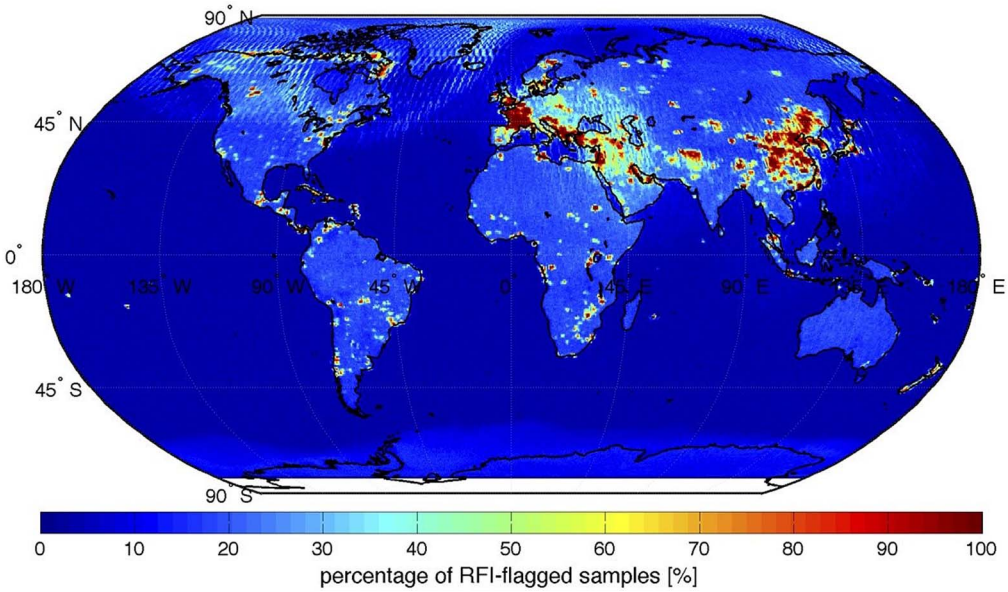

Fig. 3. Global distribution of RFI at the L-band. Percentage of samples flagged as RFI. Average of both polarization $(V + H)/2$ and all beams. August 25, 2011–August 29, 2012.

mitigation algorithm, the RFI-free short accumulations in 12 such subcycles are averaged to produce a 1.44-s data block that is passed on for additional processing. The salinity retrieval algorithm operates on this 1.44-s data block. A record of both the original unfiltered data and the RFI-free data is kept in the data file. A record is also kept of the samples removed so that one can compute statistics such as the frequency and level of RFI in a given pixel.

The 120-ms subcycle and even the 1.44-s data block are short compared with the Nyquist time for surface pixels used for mapping salinity. The along-track axes of the ellipse representing the radiometer 3-dB footprint on the surface are about 76, 84, and 96 km for the inner, middle, and outer beams, respectively [1]. Assuming an orbital velocity of 7.5 km/s and Nyquist sampling of one-half footprint, the along-track Nyquist sampling interval is 5 s or more. Given that there are 60 data samples within each 1.44-s data block, there are more than 200 data samples per Nyquist sample. Given the low sensitivity of the radiometer noise-equivalent delta temperature (NEDT) to the number of samples (i.e., NEDT varies as the square root of the number of samples [15]), a large number of samples can be lost to RFI before the radiometer performance is compromised. For example, a loss of 75% of the samples to RFI will double the NEDT.

III. Global Distribution of RFI

As of the writing of this paper, Aquarius is functioning well, producing calibrated maps of brightness temperature and credible maps of sea surface salinity [3], [16], [17]. RFI has been detected over both land and ocean. The RFI over the ocean is much less in both extent and magnitude than over land and has not prevented the retrieval of salinity in most parts of the ocean. However, over land areas of severe RFI are persistent and, in some cases, threaten applications such as the retrieval of soil moisture.

Figs. 3 and 4 illustrate the distribution of RFI detected by Aquarius. Fig. 3 shows the percentage of samples (short accumulations) flagged as RFI for a period of one year (from August 25, 2011 to August 29, 2012). Since Aquarius is in an exact repeat orbit, this provides a map of the relative frequency of RFI (or, approximately, the probability of RFI) at the geographic location of each footprint. Fig. 4 is a plot of the corresponding amplitude of the detected RFI. The amplitude is defined to be the difference between the antenna output, TA, before RFI detection and the value, TF, after the removal of samples identified as RFI. Each parameter, i.e., TA and TF, is the average value in the 1.44-s data block, and each data block is associated with a grid point on the ground (at the beam center). The data are collected for one year, and the values at each grid point are averaged over the year. In both Figs. 3 and 4, the RFI detected in the two polarizations, i.e., V and H, is averaged together for each radiometer beam, and all three beams are plotted together to give complete global coverage.

Some features of these two maps are not surprising. For example, the Distant Early Warning (DEW) line of radars [18] at the top of North America stand out (a horizontal east–west line of red blotches). In addition, in South America, most of the strong RFI is associated with major population centers. For example, Buenos Aires on the east coast of South America and Santiago on the west coast of South America stand out. Moreover, further north, an arc associated with some of the major cities of Brazil, starting with San Paolo on the east coast and Brasilia further inland, is clearly visible. Western Europe and Eastern Asia stand out for the prominent presence of RFI in these regions. The radiometers also detect RFI at locations other than at the geographic location of the sources of the RFI. An example is the halo of RFI in North America, which can be seen over the ocean in the North Atlantic starting east of Greenland and curving southwestward toward the east coast of North America and just south of Newfoundland (evident in both Figs. 3 and 4 but perhaps easiest to identify in Fig. 3).

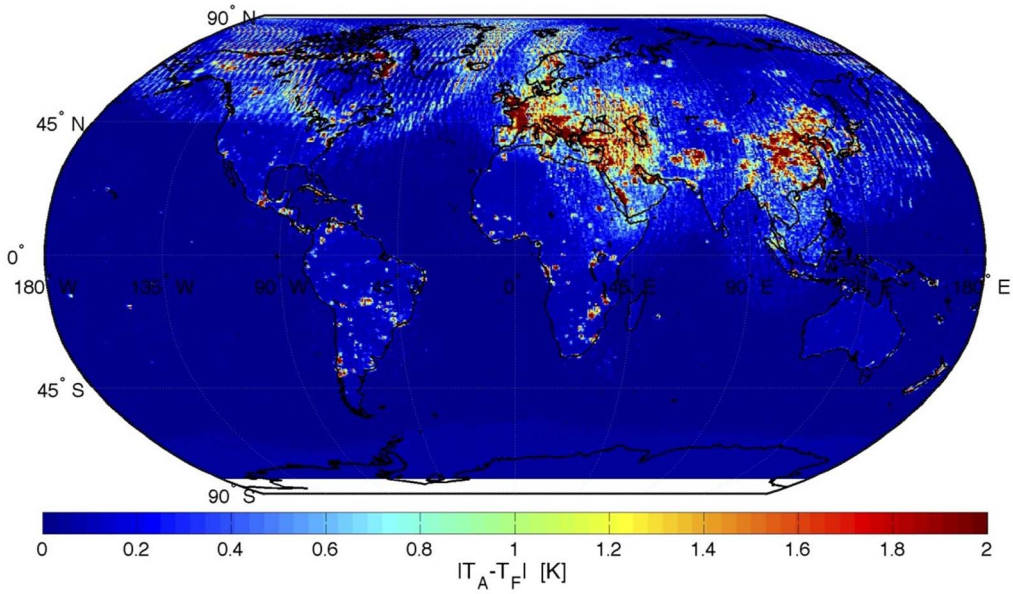

Fig. 4. Global distribution of amplitude of RFI. The difference between the radiometer output before (TA) and after (TF) removal of RFI is plotted. This is the average value for one year (from August 25, 2011 to August 29, 2012) and for both polarizations: $(\mathrm{V}+\mathrm{H})/2$. All three beams are used in the plot.

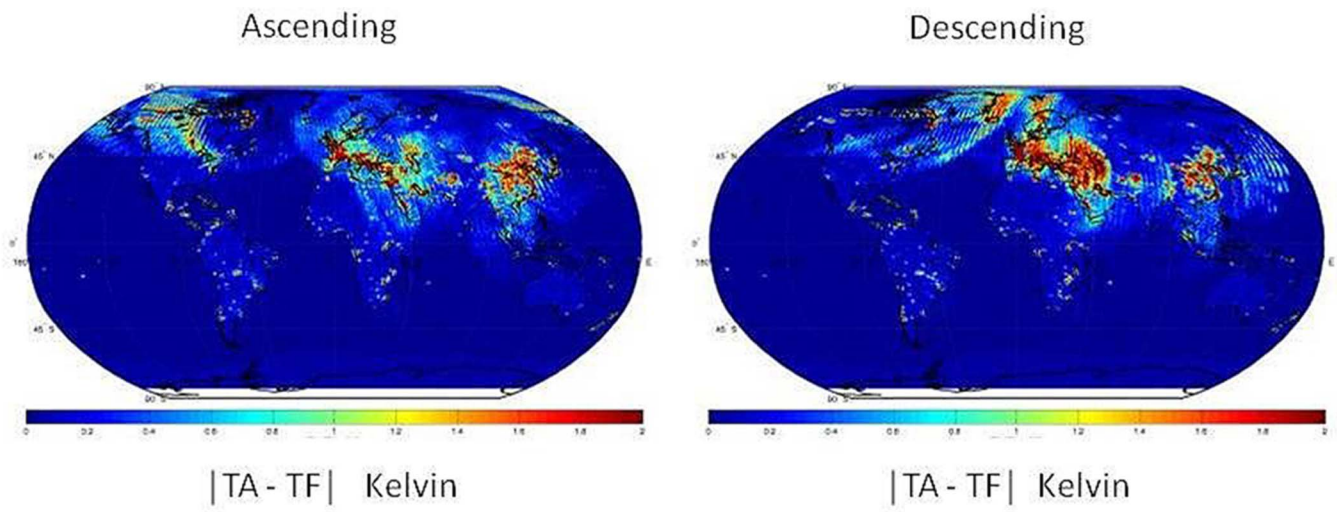

Fig. 5. Amplitude of RFI for ascending orbits (left) and descending orbits (right). One year of data, August 25, 2011–August 29, 2012, both polarization: $(\mathrm{V}+\mathrm{H})/2$ and all beams.

These RFI are most likely not due to sources in the ocean but due to strong signal from sources on land (e.g., the DEW line radars) that enter through the antenna sidelobes. Evidence of this is that the location and strength of the signal significantly varies with the polarization and orientation. This is illustrated in Fig. 5, which shows the same data as in Fig. 4 but separated into ascending (left) and descending (right) orbits. Notice that the arc of interference is more pronounced in the case of the descending orbits. The radiometers view a fixed point on the ground with different azimuth on ascending and descending orbits (e.g., see the plot of Aquarius ground tracks in Fig. 1). If the sources of RFI were located at the beam center and isotropically radiated, the detected RFI would appear similar for ascending and descending orbits; however, if the RFI were due to sources elsewhere and the radiation was entering via the antenna sidelobes, then one would expect substantial differences. This is because small changes in the orientation of the antenna can result in large changes in the sidelobes in a particular direction.

Another example can be seen in Fig. 4 in the Pacific Ocean east of China. Comparing this region in Fig. 3 (frequency of occurrence) and Fig. 4 (amplitude) suggests that this is relatively low level (low amplitude) RFI, which occurs relatively infrequently. The different appearance of this region for ascending and descending orbits seen in Fig. 5 suggests that the RFI is the result of sources elsewhere (e.g., over land probably associated with the red areas). In comparison, Fig. 3 suggests that the arc of RFI in the North Atlantic is more persistent (because the frequency as indicated in Fig. 3 is higher). Among the most troubling revelations of maps such as these is the strong persistent RFI over parts of Europe, the Middle East, and Eastern Asia. These are areas where the RFI is sufficiently

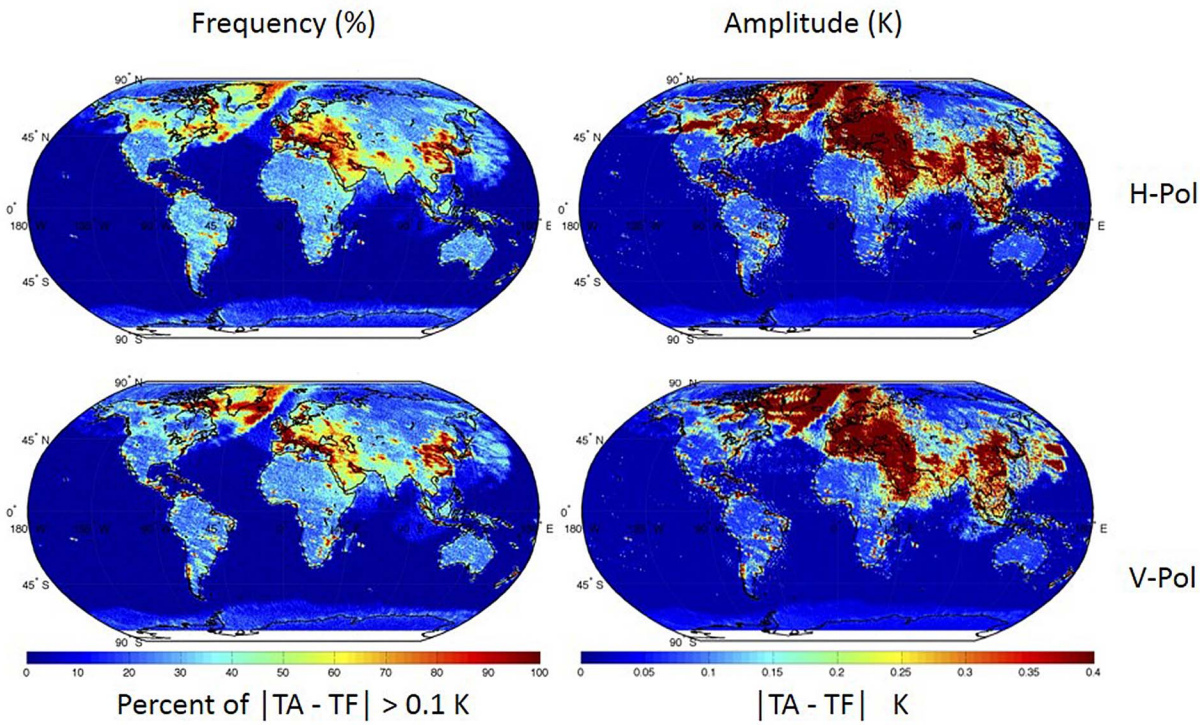

Fig. 6. One year of data for the middle Aquarius beam separated by polarization (horizontal polarization at the top and vertical polarization at the bottom) and for descending orbits only. RFI frequency is on the left, and RFI amplitude is on the right.

strong to threaten applications such as the measurement of soil moisture. This has been a source of much concern for SMOS [7], [19] and is a potential problem for future missions to measure soil moisture such as the Soil Moisture Active Passive (SMAP) mission [20], [21].

The stripes, evident for example in Fig. 4 in the halo around North America, are an artifact of the display. There are three Aquarius radiometer beams with parallel ground tracks separated by about 100 km. The way RFI is indicated is to place a color-coded "dot" at each sample point along the ground track. In places where the RFI is consistent among the beams, these points give a uniform appearance; however, when the RFI is weak and variable, it is possible to see evidence of the individual ground tracks (e.g., if the RFI appears in one beam but not in the other two beams). This can be avoided, but there is a trade between resolution and artifacts such as the stripes.

Fig. 6 illustrates the dependence of the observed RFI on the polarization of the radiometer antenna. Shown in Fig. 6 is one year of data (August 25, 2011–August 25, 2012) for the inner Aquarius beam and for descending orbits. On the left is the frequency of occurrence of the RFI and on the right the amplitude. The top row is for horizontal polarization, and the bottom row is for vertical polarization. The large-scale patterns of RFI are very similar to those in Figs. 3 and 4. However, there are subtle differences as a function of polarization, for example, in the details of the halo discussed above in the North Atlantic associated with the DEW line (at about 80° N latitude) and the RFI in the Western Pacific off the coast of China. Difference maps indicate that, in general, the differences are not large. The differences in frequency for the two polarizations (Fig. 6, left) are on the order of ±15% with nearly zero difference over the ocean and a negative bias over land (but the algorithm is tuned for operation over the ocean and the parameters in Table I have not yet been adjusted to rule out a difference in the false-alarm rate over land). The most significant discernible feature associated with frequency of occurrence (Fig. 6, left) is associated with the DEW line in North America. The differences in the case of amplitude (Fig. 6, right) reflect the strong sources of RFI (i.e., the strongest differences in amplitude correspond to the areas in red in Figs. 4 and 6). It appears that stronger sources are more likely to produce larger differences in amplitude between V- and H-polarizations. However, this may just be an issue of scale as stronger sources are capable of producing bigger difference and requires a more detailed investigation. The DEW line and the strong RFI off the coast of China were associated with discernible differences in amplitude, as can be seen in Fig. 6 (right).

The purpose of the Aquarius RFI detection and mitigation algorithm is to detect and remove RFI that has the potential to corrupt the retrieval of sea surface salinity regardless of

TABLE I
ALGORITHM PARAMETERS

Beam		σ_s		τ_m	τ_d	W_m	W_d
		Vertical	Horizontal				
Inner		0.558	0.532	1.5	4	20	2
Middle		0.543	0.538	1.5	4	20	2
Outer		0.552	0.546	1.5	4	20	2

$T_m = \tau_m \sigma_s g$ $T_d = \tau_d \sigma_s g$

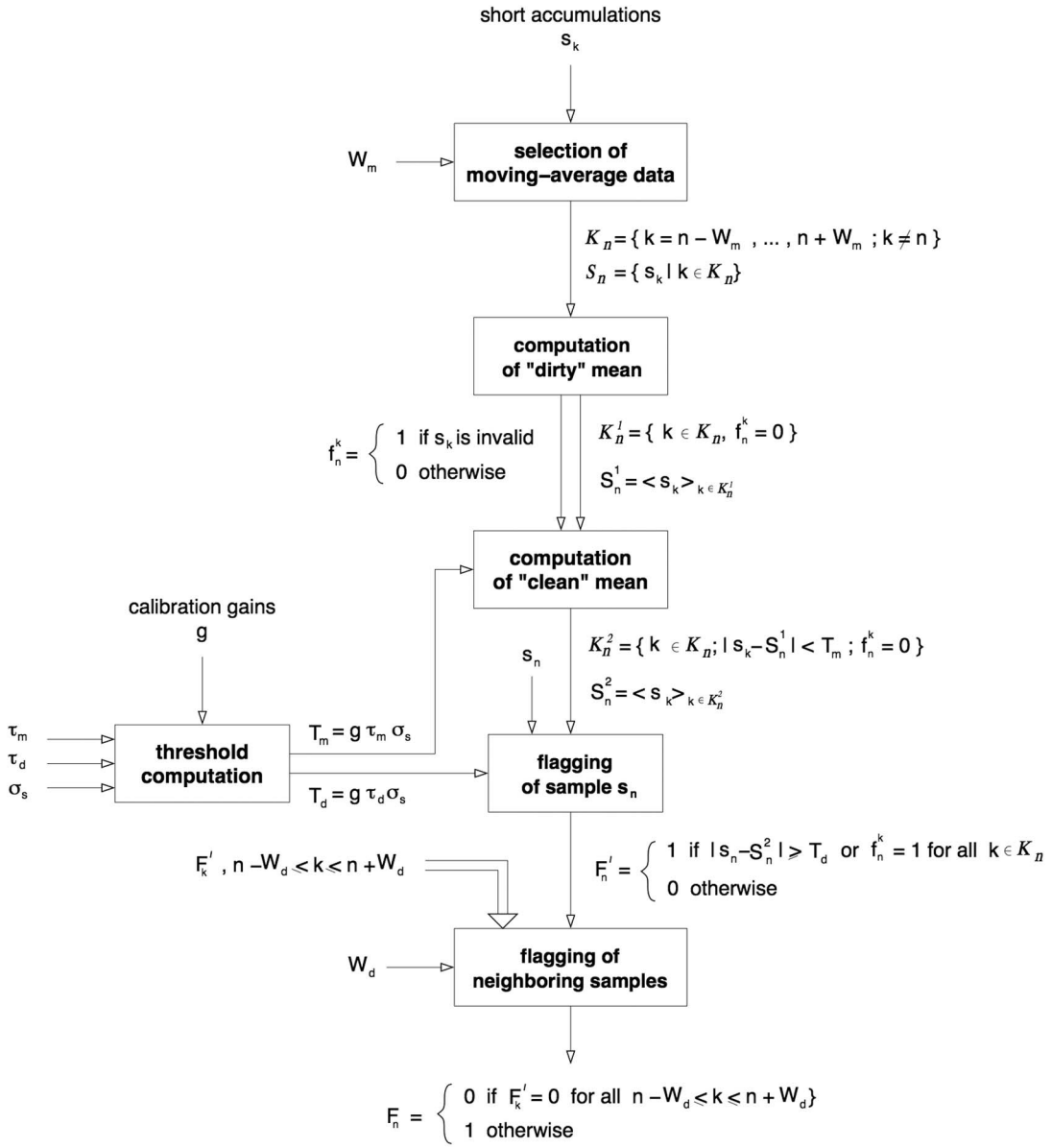

Fig. 7. Flow diagram for the Aquarius RFI detection algorithm.

the location of its source. In this respect, it appears to be working well as Aquarius is producing reasonable maps of surface salinity [3], [15], [16]. The remainder of this paper is focused on describing the algorithm and reporting performance metrics such as the false-alarm rate, which are important for understanding the consequence of this approach and for choosing parameters to optimize the algorithm. The parameters of the algorithm were set prelaunch, and it is clear from analysis of the data that the algorithm can be improved by tuning the parameters and by having a different set of parameters for land and ocean applications.

IV. Detection Algorithm

The Aquarius RFI detection algorithm [10] is an adaptation of an earlier algorithm [11] designed to detect pulsed interference such as is expected from a radar. Experience with ground-based sensors indicated that the air traffic control radar was a significant source of RFI in the protected band at 1.413 GHz [4], [5]. The algorithm is a glitch detector in the sense that it compares a sample under test with a local mean obtained from neighboring samples, and it rejects the sample if it deviates too much from a local mean [10].

The steps in the RFI detection algorithm as implemented for Aquarius are illustrated in Fig. 7. First, a string is formed of the raw data samples (short accumulations). This is done in integer steps (one for each 10 ms) with zeros applied when there are no antenna measurements such as occurs during the intervals of internal calibration (see Fig. 2). The first two short accumulations, which represent 20 ms of data, are divided by 2 and counted twice. For each subcycle of 120 ms, the result is a string of values s_n with $n = \{1, 2, \ldots, 7\}$ representing the short accumulations followed by five zeros, $s_n = 0$ for $n = \{8, 9, 10, 11, 12\}$, representing the intervals devoted to calibration. There are 12 such cycles in each 1.44-s block comprised of $84 = 12 \times 7$ nonzero samples. All the strings are lined up in

temporal order to form a continuous stream of values that are then used by the RFI detection algorithm.

The test for RFI is applied to each nonzero sample, s_n, in this stream (i.e., each value that corresponds to an antenna measurement). The algorithm consists of the following steps (see Fig. 7).

1) Computation of a "dirty" mean: A "dirty" mean is computed using all samples s_k within $\pm \mathrm{W}_m$ steps of the sample s_n under consideration (i.e., samples between $s_n \pm \mathrm{W}_m$ counting zeros). In the current implementation of Aquarius $\mathrm{W}_m = 20$ steps. The dirty mean is the mean value of the nonzero elements among these 41 samples.
2) Computation of a "clean" mean: All samples that differ from the dirty mean by a preset threshold, T_m, are dropped (only for this step), and a new mean is computed (again ignoring zeros). The new mean is called the "clean" mean and is the basis for deciding if the sample being examined, s_n, is RFI.
3) Flagging samples: The sample s_n is compared with the clean mean. If it differs from this mean by more than a preset threshold, T_d, then it is considered to be RFI and flagged. In addition, samples within $\pm \mathrm{W}_d$ steps on either side of s_n (counting zeros) are considered tainted and also flagged as RFI. $\mathrm{W}_d = 2$ in the current algorithm, which means that all samples between $s_{n\pm2}$ are considered to be RFI whenever s_n is identified as RFI.

RFI mitigation begins once the process in steps 1–3 above has been applied to each s_n in the data stream. The data stream is partitioned into blocks of 1.44 s (12 subcycles consisting of 12×7 nonzero samples). RFI mitigation consists of removing from this block all samples flagged as RFI. If there are no RFI detected, $12 \times 7 = 84$ samples will be averaged together to produce one data point. If RFI is detected, those samples flagged are removed, and the remaining values are averaged. The average value before mitigation (i.e., including all 84 samples regardless of RFI) is called TA, and the average value after removal of samples identified as RFI is called TF.

Quality flags are issued to identify when the number of samples removed is sufficiently large to have a significant impact on the effective radiometer NEDT for the 1.44-s average. (This is done assuming independent samples, and a flag is issued if the effective NEDT increases by a factor of 2 or more.) A record is also kept of the number of samples included in the average.

The thresholds $\mathrm{T}_m = \tau_m \sigma_s g$ and $\mathrm{T}_d = \tau_d \sigma_s g$ used in steps 2 and 3 have been chosen on the assumption that the radiometer output is normally distributed with a mean equal to the clean mean and a standard deviation close to the NEDT of the radiometer. The values currently used in the algorithm for these parameters are listed in Table I. The values of g and σ_s were chosen based on Aquarius radiometer performance measured after launch, as described below. The values of τ and W were chosen based on prelaunch studies of the algorithm, as described in [10]. Parameter σ_s is intended to be representative of the radiometer NEDT. It is adjustable, and it was estimated prelaunch from laboratory test data. Values were separately established for each radiometer, but the same value was used for both polarizations (V, H) in each radiometer. The prelaunch values (all on the order of 0.5 K) were modified after launch based on the observed radiometer performance (i.e., looking at the radiometric noise over a relative constant ocean scene far from land where RFI was likely to be very small). The choice of σ_s has a significant impact on the false-alarm rate (as will be discussed further below), and research is underway to tune this parameter for optimum performance using values appropriate for the scene (e.g., different values for land and ocean). Parameters τ_d and τ_m set the width of the filter in terms of the standard deviation of noise (i.e., σ_s). They are also adjustable. A low value of τ_d increases the false-alarm rate (identifying a sample as RFI when it is not), whereas an overly high value increases the likelihood that a sample is corrupted by RFI but is not identified as such. The parameter, τ_m, used in the case of the "dirty" mean is less critical because it does not result in lost data. It is only used to exclude data during the computation of the clean mean, and those excluded values are replaced in the final processing. Finally, parameter g is the radiometer gain. It appears in the expressions for T_m and T_d as a scale factor because the algorithm is designed to act on the radiometer counts (i.e., before calibration). The calibration is done in a separate processing block, and the values for the gain g used in the conversion from counts to Kelvin are handed to the RFI filter from this processing module.

After launch, it was noticed that the first short accumulation was unusually noisy and biased relative to the other samples. The reason for this has not yet been confirmed but appears to be associated with a switch. The impact of this behavior was sufficient to bias the algorithm and significantly increase the false-alarm rate. Consequently, this sample is not currently being included in the data stream. It has been replaced by zeros in the RFI detection algorithm, and this measurement is no longer used in the salinity retrieval. The examples presented here have been generated with this sample removed, and it has not been part of the Aquarius data stream since late summer of 2011. The impact of removing this sample from the data stream on the radiometer effective NEDT is small (i.e., on the order of $(7/5)^{1/2} = 1.18$ assuming independent samples), and the radiometer NEDT is a small element in the error budget for the salinity retrieval [2].

V. Discussion

A. Detection of RFI

Technically, RFI is detected each time a sample s_n exceeds the threshold, T_m, for a particular radiometer channel (e.g., V-pol or H-pol). The remaining samples are aggregated to form an average value every 1.44 s. One way to look at the level of RFI is to compare the 1.44-s average antenna temperature before removal of RFI (called TA) and after removal of RFI (called TF). The difference is due to RFI and represents the net contribution of RFI in the 1.44-s window. Figs. 4–6 (right) are plots of this difference. Fig. 4 shows the magnitude of this difference as a function of location averaged over both polarizations. The level for each location is the average value at that location for one year of observations. Fig. 5 shows the same information but separated into ascending and descending

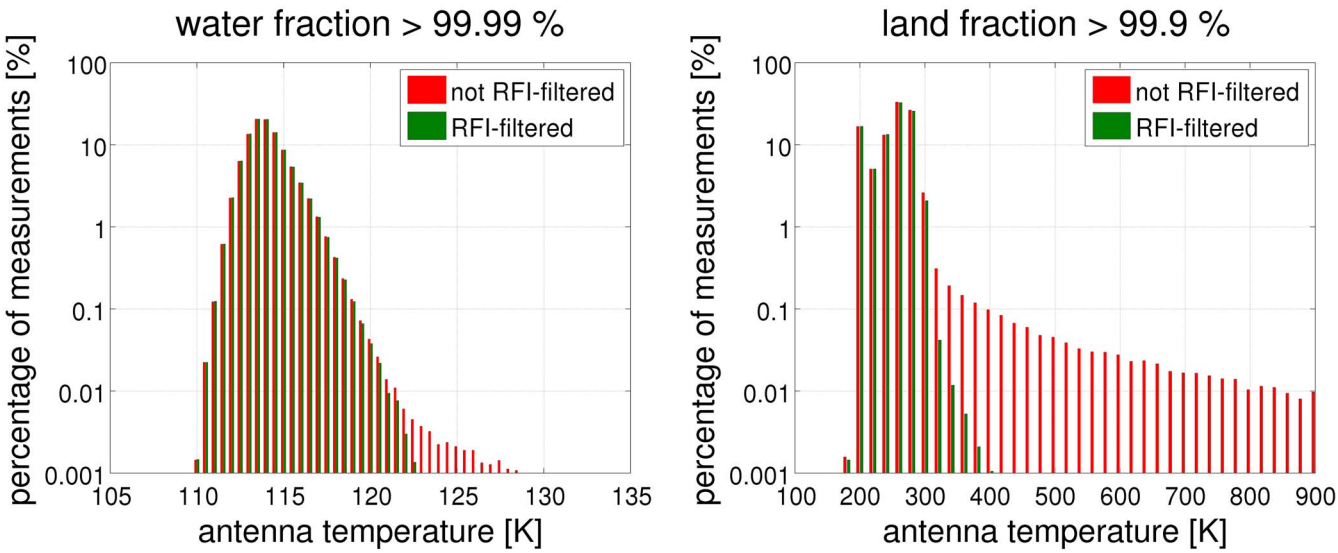

Fig. 8. Histograms of antenna temperature before RFI removal (TA) and after RFI removal (TF). These data are for the middle Aquarius beam and vertical polarization. Data for one year are shown (August 25, 2011–August 24, 2012). The figure on the left is for ocean only, and the figure on the right is for land only.

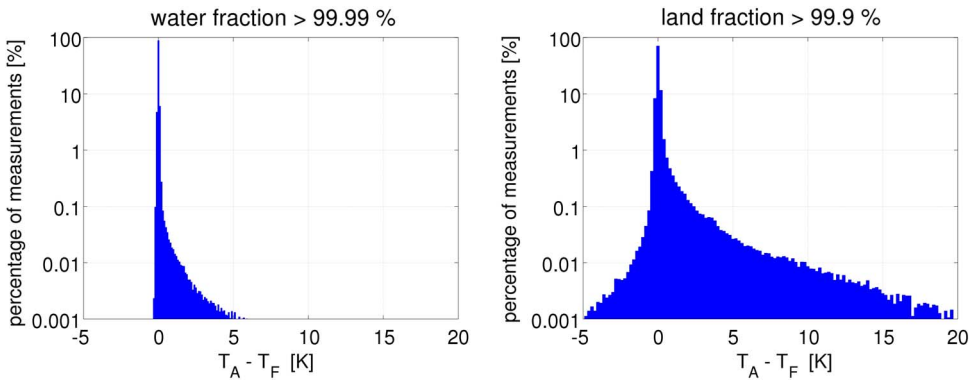

Fig. 9. Histograms of the difference TA–TF of the antenna temperature before RFI removal (TA) and after RFI removal (TF). These data are for the middle Aquarius beam and vertical polarization. Data for one year are shown (August 25, 2011–August 25, 2012). The figure on the left is for ocean only, and the figure on the right is for land only.

orbits, and the right-side panel in Fig. 6 shows the magnitude of this difference separately for each polarization, for the Aquarius middle beam, and only for the descending orbits. The RFI entering from the sidelobes can be distinguished by its strong dependence on polarization and orientation.

Another way to look at the detected RFI is to consider the histograms of the antenna temperature before and after removal of RFI (i.e., histograms of TA and TF, respectively). Examples are shown in Fig. 8 for one year of data (from August 25, 2011 to August 24, 2012). TA is shown in red and TF in green. The ordinate is the percent of the measurement, and the abscissa is the value of TA or TF, as appropriate. The histogram on the right is for land only (land fraction greater than 99.9%), and the histogram on the left is for ocean only (water fraction greater than 99.99%). The data in both cases are for the middle Aquarius beam (37.8° local incidence angle) and vertical polarization. The histograms illustrate the limitations of using a fixed threshold alone to detect RFI. For example, assume a threshold of 320 K. Then, looking at the histogram for land (right), all values of TA (red) exceeding 320 K would be labeled as RFI. These "RFI" could easily be detected with a simple threshold filter. However, they are relatively rare occurrences (less than 0.1%). Furthermore, for antenna temperatures that are accepted in this example (i.e., TA $<$ 320 K), TA occurs slightly more often than TF for a given value of antenna temperature. This suggests that the more common level of RFI is that which does not drive the antenna temperature out of the normal range. This is the regime where the skill of the RFI detection algorithm is evident and where a simple threshold (i.e., TA $>$ TA_0) would miss many instances of interference. The true value of the algorithm is in identifying these more subtle differences between TA and TF that occur at what would otherwise appear to be reasonable values over both land and ocean.

This is illustrated in Fig. 9, which is a histogram of the difference TA–TF. It is for the same data as in Fig. 8 with water fraction greater than 99.99% on the left and land fractions greater than 99.9% on the right. The percent of occurrence is on the ordinate but this time grouped along the abscissa as the difference between TA and TF. The difference, i.e., TA–TF, is an indication of the level (amplitude) of the RFI, and the origin TA–TF signifies no RFI. It is clear from these histograms that much of the RFI is small in amplitude. This is the range where sensitive RFI detection and mitigation capability is important

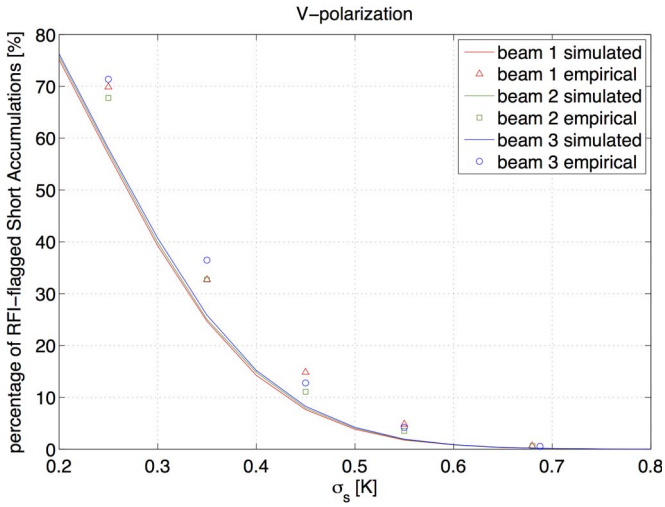

Fig. 10. False-alarm rate as a percent of signal as a function of the standard deviation, i.e., σ_s, used to determine the algorithm detection threshold. (Solid line) Theory. (Colored symbols) Measurements using Aquarius data over ocean.

because even with RFI present, the TAs appear to be of reasonable amplitude. (Note that the histogram is for the level of detected RFI, which, as explained above, is not the same as the level of the signal at the source of the RFI.)

Notice the occurrence of negative values of TA–TF in Fig. 9. This is a peculiarity of the detection algorithm. The algorithm is double-sided and discards values that deviate from the mean because they exceed the threshold by being too large or too small. A double-sided algorithm is used to avoid introducing a calibration bias when only false alarms are present. However, as a consequence, it is possible to have TF $>$ TA when small values are identified as RFI. TF and TA are the average over all the samples in 1.44 s; hence, if the algorithm flags as RFI values on the low side of the mean more often than on the high side, the average TF can be larger than the average TA (which includes more small values). It is evident from the histograms that this does not happen very often. One can argue that, at least in part, this is not really RFI but a component of the algorithm false-alarm rate (see Section V-B).

Another peculiarity of the algorithm is the existence of values of TF larger than one would expect to encounter over land (e.g., values between 300 K and 400 K in Fig. 8). These rarely occur (less than 0.1%) and are evidence of misdetection in the algorithm.

B. False-Alarm Rate

The Aquarius glitch detection algorithm has an inherent false-alarm rate. This is because the criterion for identifying a signal as RFI is that it exceeds a threshold, and given the stochastic nature of the output of a radiometer, there is always some nonzero probability that the natural signal (i.e., with no RFI) will exceed this threshold. The false-alarm rate is simply the probability that the signal, s_n, will exceed the threshold when no RFI is present.

A discussion of the false-alarm rate for this type of glitch detection algorithm can be found in [10]. Fig. 10 illustrates how the algorithm, as currently implemented for Aquarius, compares with theory. The figure shows the percent of signal falsely identified as RFI as a function of parameter σ_s used in the algorithm. The solid curve is the theoretical value computed with all other parameters fixed at the values currently used in the Aquarius implementation (see Table I). It is obtained by generating normally distributed random noise and running it through the RFI detection algorithm. There are three curves, one for each Aquarius radiometer beam. The mean of the noise is set to zero (for convenience), and the standard deviation is set to the value obtained from the Aquarius radiometer data. As σ_s in the algorithm increases (abscissa in the plot), the effective threshold, $\mathrm{T}_d = g\tau_m\sigma_s$, used in the RFI algorithm to determine that a signal is RFI also increases. The false-alarm rate is the fraction of signal exceeding this threshold. In the case of a normal distribution (Gaussian), the false-alarm rate is the error function, $\mathrm{erf}(\mathrm{T}_d)$, and it decreases as T_d increases. In the case of this simulation, T_d increases proportional to σ_s, and the false alarm decreases with increasing σ_s, as can be seen in the figure. There is an obvious trade to be made between making the threshold too large (in which case, one gets a small false-alarm rate, but only very strong RFI are detected) or making the threshold very small (in which case, the algorithm is very sensitive to RFI but has a large false-alarm rate). That is, there is a trade to be made between the false-alarm rate and the rate of missed detection.

The colored symbols in Fig. 10 represent actual observations from Aquarius. These points have been obtained using Aquarius measurements collected over the ocean far from land and then processing the data through the RFI algorithm and recording the percent of samples, s_n, identified as RFI. The assumption is that in the open ocean far from land, the likelihood of encountering man-made sources of signal is low, and consequently, the signal identified as RFI is likely to be a false alarm. Clearly, this is an approximation, but as can be seen in Fig. 10, the results (the symbols) are in reasonable agreement with the prediction (the solid lines). Several cases are shown in Fig. 10 (the five clusters of symbols). These were obtained by processing the data through the algorithm with the different values of σ_s. The values used in the present operational algorithm are shown in Table I and correspond to the cluster of symbols near $\sigma_s = 0.55$ and a false-alarm rate of better than 5%.

The data in Fig. 10 show a somewhat higher percentage of detection than theory. One possible reason is that there is probably some low-level RFI present. In addition, the Gaussian model for the distribution of TA is only an approximation. It is also likely to change when RFI is present. Given the level of approximation, it is encouraging that the experimental results are as close as they are to the model. The examples shown in Fig. 10 are for vertical polarization. The situation for horizontal polarization is similar, although the agreement is somewhat poorer, particularly in the case of the outer beam.

False-alarm rates at the level indicated in Fig. 10 for the current algorithm (i.e., 5% or less) are not a significant concern for Aquarius. The effect of eliminating good data due to the false-alarm rate is to increase the effective NEDT of the radiometers. However, because of extensive oversampling, a lot of data can be lost to RFI before there is a significant impact on the

effective NEDT of the data. For example, the Nyquist rate for the Aquarius antennas is on the order of 5–6 s (assuming a nominal velocity of 7.5 km/s and a cross-track width of 76–96 km [1]). This corresponds to more than 200 individual 10-ms samples, s_n, in each independent pixel ($[5/1.44] \times 60 = 200$). Losing 10% to the false-alarm rate corresponds to an increase in about 1.05 in the effective NEDT. The effective NEDT of the radiometers in 6 s is on the order of 0.06 K [1], and it is only a very small part of the total error budget for the retrieval of salinity [2].

VI. Conclusion

Initial indications are that the Aquarius algorithm for detection and mitigation of RFI is working well. The global distribution of detected RFI correlates well with population centers and likely sources such as the DEW line of radars. The algorithm appears to have modest rates for false alarms based on data collected over the ocean where it is easiest to evaluate these performance metrics. Of course, the level of RFI is low over the ocean, and an evaluation of its performance when RFI is strong and persistent as occurs in several places over land remains to be done.

The algorithm contains several tunable parameters (e.g., the thresholds for identifying a signal as RFI), and as of the writing of this paper, the algorithm uses parameters tuned to performance over the ocean. These parameters are currently the subject of investigation and will be adjusted to improve performance over land and, eventually, to seek an optimum trade between false alarm and missed detection. The RFI observed over land is more prevalent and stronger, but the applications over land such as for monitoring soil moisture are also more tolerant of noise than over the ocean for the retrieval of salinity. Quantifying the missed-detection rate and determining optimum parameters suitable for the different applications over land and ocean are the focus of current research by the authors.

The frequency of occurrence maps (e.g., Fig. 3) agree well with the maps produced by SMOS [7] (also see: http://www.cesbio.ups-tlse.fr/SMOS_blog/?tag=rfi). However, there are some significant differences. For example, SMOS is no longer showing the high percentage of RFI over France and the DEW line that are still evident in the Aquarius maps. This is being investigated, and among the potential reasons are differences in radiometric sensitivity, difference in the effective passband of the receivers, and differences in algorithm thresholds.

Finally, the Aquarius RFI detection and mitigation algorithm is only one step in the evolution of processors for L-band radiometers to deal with RFI. While it appears to be working well over ocean, there is still work to be done to establish a missed-detection rate and to evaluate its performance over land where the RFI is stronger and more varied. The next generation, represented by SMAP [20], [21], will soon be in space. It will employ significantly more sophisticated processing to permit the application of kurtosis and subbanding to mitigate RFI [21]. Ideally, SMOS, Aquarius, and SMAP will someday fly together and, by intercomparison, help establish performance metrics for the different techniques.

References

[1] D. M. Le Vine, G. S. E. Lagerloef, F. R. Colomb, S. H. Yueh, and F. A. Pellerano, "Aquarius: An instrument to monitor sea surface salinity from space," *IEEE Trans. Geosci. Remote Sens.*, vol. 45, no. 7, pp. 2040–2050, Jul. 2007.

[2] G. S. E. Lagerloef, F. Colomb, D. Le Vine, F. Wentz, S. Yueh, C. Ruf, J. Lilly, J. Gunn, Y. Chao, A. deCharon, G. Feldman, and C. Swift, "The Aquarius/SAC-D mission: Designed to meet the salinity remote sensing challenge," *Oceanography*, vol. 21, no. 1, pp. 68–81, Mar. 2008.

[3] D. M. Le Vine, G. S. E. Lagerloef, C. Ruf, F. Wentz, S. Yueh, J. Piepmeier, E. Lindstrom, and E. Dinnat, "Aquarius: The instrument and initial results," in *Proc. Microrad*, Frascati, Italy, Mar. 2012, pp. 1–3.

[4] D. M. Le Vine, "ESTAR experience with RFI at L-band and implications for future passive microwave remote sensing from space," in *Proc. IEEE IGARSS*, Toronto, ON, Canada, Jun. 24–28, 2002, vol. 2, pp. 847–849.

[5] D. M. Le Vine and M. Haken, "RFI at L-band in synthetic aperture radiometers," in *Proc. IEEE IGARSS*, Jul. 21–25, 2003, vol. 3, pp. 1742–1744.

[6] N. Skou, S. Misra, J. E. Balling, S. S. Kristensen, and S. S. Sobjaerg, "L-band RFI as experienced during airborne campaigns in preparation for SMOS," *IEEE Trans. Geosci. Remote Sens.*, vol. 48, no. 3, pp. 1398–1407, Mar. 2010.

[7] R. Oliva, E. Daganzo, Y. Kerr, S. Mecklenburg, S. Nieto, P. Richaume, and C. Gruhier, "SMOS radio frequency interference scenario: Status and actions taken to improve the RFI environment in the 1400–1427-MHz passive band," *IEEE Trans. Geosci. Remote Sens.*, vol. 50, no. 5, pp. 1427–1439, May 2012.

[8] N. Skou, J. E. Balling, S. S. Sobjarg, and S. S. Kristensen, "Surveys and analysis of RFI in the SMOS context," in *Proc. IEEE IGARSS*, Jul. 25–30, 2010, pp. 2011–2014.

[9] D. M. Le Vine, G. S. E. Lagerloef, and S. E. Torrusio, "Aquarius and remote sensing of sea surface salinity from space," *Proc. IEEE*, vol. 98, no. 5, pp. 688–703, May 2010.

[10] C. Ruf and S. Misra, "Detection of radio-frequency interference for the Aquarius radiometer," *IEEE Trans. Geosci Remote Sens.*, vol. 46, no. 10, pp. 3123–3128, Oct. 2008.

[11] N. Niamsuwan and J. T. Johnson, "Examination of a simple pulse-blanking technique for radio frequency interference mitigation," *Radio Sci.*, vol. 40, no. 5, pp. RS5S03-1–RS5S03-11, Oct. 2005.

[12] S. H. Yueh, R. West, W. J. Wilson, F. K. Li, E. G. Njoku, and Y. Rahmat-Samii, "Error sources and feasibility for microwave remote sensing of ocean surface salinity," *IEEE Trans. Geosci Remote Sens.*, vol. 39, no. 5, pp. 1049–1059, May 2001.

[13] F. A. Pellerano, J. Piepmeier, M. Triesky, K. Horgan, J. Forgione, J. Caldwell, W. J. Wilson, S. Yueh, M. Spencer, D. McWatters, and A. Freedman, "The Aquarius ocean salinity mission high stability L-band radiometer," in *Proc. IEEE IGARSS*, Jul./Aug. 2006, pp. 1681–1684.

[14] E. P. Dinnat and D. M. Le Vine, "Impact of sun glint on salinity remote sensing: An example with the Aquarius radiometer," *IEEE Trans. Geosci. Remote Sens.*, vol. 46, no. 10, pp. 3137–3150, Oct. 2008.

[15] F. T. Ulaby, R. K. Moore, and A. K Fung, *Microwave Remote Sensing*. Reading, MA, USA: Addison-Wesley, 1981, sec. 6.7.

[16] G. S. E. Lagerloef, "Satellite mission monitors ocean surface salinity," *Trans. Amer. Geophys. Union*, vol. 93, no. 25, pp. 233–234, Jun. 2012.

[17] T. Lee, G. Lagerloef, M. Gierach, H.-Y. Kao, S. Yueh, and K. Dohan, "Aquarius reveals salinity structure of tropical instability waves," *Geophys. Res. Lett.*, vol. 39, no. 12, pp. L12610-1–L12610-6, Jun. 2012.

[18] F. R. Naka and W. W. Ward, "Distant early warning line radars: The quest for automatic signal detection," *Lincoln Lab. J.*, vol. 12, no. 2, pp. 181–204, 2000.

[19] Y. H. Kerr, P. Waldteufel, J.-P. Wigneron, S. Delwart, F. Cabot, J. Boutin, M.-J. Escorihuela, J. Font, N. Reul, C. Gruhier, S. E. Juglea, M. R. Drinkwater, A. Hahne, M. Martin-Neira, and S. Mecklenburg, "The SMOS mission: New tool for monitoring key elements of the global water cycle," *Proc. IEEE*, vol. 98, no. 5, pp. 666–687, May 2010.

[20] D. Entakhabi, E. G. Njoku, P. E. O'Neill, K. H. Kellogg, W. T. Crow, W. N. Edelstein, J. K. Entin, S. D. Goodman, T. J. Jackson, J. Johnson, J. Kimball, J. R. Piepmeier, R. D. Koster, N. Martin, K. C. McDonald, M. Moghaddam, S. Moran, R. Reichle, J.-C. Shi, M. W. Spencer, S. W. Thurman, and J. Van Zyl, "The Soil Moisture Active Passive (SMAP) mission," *Proc. IEEE*, vol. 98, no. 5, pp. 704–716, May 2010.

[21] D. Bradley, C. Brambora, M. E. Wong, L. Miles, D. Durachka, B. Farmer, P. Mohammed, J. Piepmier, J. Medeiros, N. Martin, and R. Garcia, "Radio-Frequency Interference (RFI) mitigation for the Soil Moisture Active/Passive (SMAP) radiometer," in *Proc. IEEE IGARSS*, Jul. 2010, pp. 2015–2018.

David M. Le Vine (M'70–SM'79–F'95–LF'07) received the Ph.D. degree in electrical engineering from the University of Michigan, Ann Arbor, MI, USA. His educational background is electrical engineering with specialization in electromagnetic theory and physics.

He is currently with the Earth Sciences Division, NASA's Goddard Space Flight Center, Greenbelt, MD, USA, where he does research to develop techniques for microwave remote sensing of the environment from space. He was a faculty member with the Department of Electrical Engineering, University of Maryland, College Park, MD, USA, and an adjunct faculty member with The George Washington University, Washington, DC, USA. His research has focused on passive remote sensing at the long wavelength end of the microwave spectrum (e.g., L-band) with applications to remote sensing of soil moisture and sea surface salinity. An example of this work is the development of the synthetic aperture radiometer, i.e., ESTAR. He is currently the Deputy Principal Investigator for AQUARIUS, a NASA Earth System Science Pathfinder mission to measure sea surface salinity. He is also a member of the Quality Working Group for ESA's Soil Moisture and Ocean Salinity mission and of the Soil Moisture Active Passive science team.

Dr. Le Vine is a member of the Geoscience and Remote Sensing Society (GRSS) and the Antennas and Propagation Society. He is currently a member of the GRSS Administrative Committee. He is also a member of the International Union of Radio Science and the American Geophysical Union.

Paolo de Matthaeis (S'96–M'04) was born in Rome, Italy. He received the Laurea degree (summa *cum laude*) in electrical engineering from the University of Rome "Tor Vergata," Rome, in 1991 and the Doctor of Science degree in electrical engineering from The George Washington University, Washington, DC, USA, in 2005.

In 1993–1994, he was with the European Space Agency, ESTEC, Noordwijk, The Netherlands, under the Young Graduate Trainee program. In 1994–1995, he received a grant from the Italian Space Agency (ASI) to carry out research in the SIR-C/X-SAR data at the Remote Sensing Laboratory, University of Rome "Tor Vergata." He is currently with the Goddard Earth Sciences Technology and Research, NASA Goddard Space Flight Center, Greenbelt, MD, USA. His research work includes active and passive microwave remote sensing, with special interest in electromagnetic modeling of vegetation and sea surface. He is part of the Science Algorithms team for the AQUARIUS instrument.

Dr. de Matthaeis is a member of the IEEE Geoscience and Remote Sensing Society and of the American Geophysical Union.

Christopher S. Ruf (S'85–M'87–SM'92–F'01) received the B.A. degree in physics from Reed College, Portland, OR, USA, and the Ph.D. degree in electrical and computer engineering from the University of Massachusetts, Amherst, MA, USA.

He is currently a Professor of atmospheric, oceanic, and space sciences; a Professor of electrical engineering and computer science; and the Director of the Space Physics Research Laboratory with the University of Michigan, Ann Arbor, MI, USA, and a Principal Investigator with the NASA Cyclone Global Navigation Satellite System Earth Venture mission. He was with Intel Corporation, Hughes Space and Communication, the NASA Jet Propulsion Laboratory, and Pennsylvania State University, University Park, PA, USA. His research interests include GNSS-R bistatic scatterometry, microwave radiometry, atmosphere and ocean geophysical retrieval algorithm development, and sensor technology.

Dr. Ruf is a member of the American Geophysical Union, the American Meteorological Society, and Commission F of the Union Radio Scientifique Internationale. He was the Editor-in-Chief of the IEEE TRANSACTIONS ON GEOSCIENCE AND REMOTE SENSING and has served on the editorial boards of *Radio Science* and the *Journal of Atmospheric and Oceanic Technology*. He was a recipient of four NASA Certificates of Recognition and seven NASA Group Achievement Awards, as well as of the 1997 TGRS Best Paper Award, the 1999 IEEE Resnik Technical Field Award, and the 2006 IGARSS Best Paper Award.

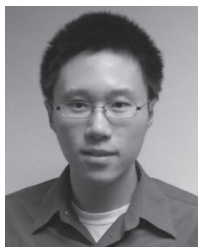

David D. Chen received the Bachelor's degree (with honors) in electrical and computer engineering from the University of Toronto, Toronto, ON, Canada. He is currently working toward the Ph.D. degree in electrical engineering at the University of Michigan, Ann Arbor, MI, USA.

His current research interests are in the fields of microwave radiometry and GNSS-R.

Mr. Chen is currently a holder of the NASA Earth and Space Science Fellowship. He was a recipient of the IEEE Antennas and Propagation Society Predoctoral Research Award in 2012, a fellowship from the Natural Sciences and Engineering Research Council of Canada (NSERC) in 2011, an NSERC Undergraduate Research Award in 2009, and an ECE Department Summer Research Fellowship in 2007.